A Field Enhancement Integration Design Featuring Misalignment Tolerance for Wireless EV Charging Using *LCL* Topology

Pengcheng Zhang, *Member, IEEE*, Maryam Saeedifard, *Senior Member, IEEE*, Omer C. Onar, *Senior Member, IEEE*, Qingxin Yang, and Changsong Cai, *Member, IEEE*

***Abstract*—This article proposes a magnetic integration design for EV wireless power transfer (WPT) systems, where the compensation and transmitting coils overlap one on top of the other to share the ferrite layer without any decoupling consideration. The magnetic field generated by both the compensation and transmitting coils are exploited to transfer power. To this end, a compensation method is proposed to enable magnetic field enhancement without any reactive power flow between the compensation and the transmitting coils, and to achieve input zero phase angle and constant current output. In addition, an efficient finite element analysis-based coil optimization algorithm is proposed to improve the coil misalignment tolerance on the horizontal plane, in which a reversely connected inner coil is used to stabilize the system output under misalignment conditions. Analytical and simulation results confirm transmission flux density enhancement and reduced leakage field characteristics of the proposed coil design. Finally, a scaled-down WPT prototype is built and tested to verify the performance and effectiveness of the design. The proposed design achieves 91.17% efficiency and misalignment tolerance up to 200 mm in any XY-direction while maintaining the power transfer and its efficiency. The results of this work provide insights into magnetic integration design of high-order compensation topologies featuring higher compactness, less ferrite usage, magnetic field enhancement, and misalignment tolerance for WPT systems.**

***Index Terms*—Field enhancement, high-order resonant network, magnetic integration, misalignment tolerance, wireless charging.**

Manuscript received April 5, 2020; revised July 21, 2020; accepted August 31, 2020. Date of publication September 3, 2020; date of current version November 20, 2020. This work was funded by the China Scholarship Council (Grant No. 201706700003) and the Major Program of the National Natural Science Foundation of China (Grant No. 51690181). Recommended for publication by Associate Editor C. K. Lee. *(Corresponding author: Changsong Cai.)*

Pengcheng Zhang is with the State Key Laboratory of Reliability and Intelligence of Electrical Equipment, Hebei University of Technology, Tianjin 300132, China, and also with the Georgia Institute of Technology, Atlanta, GA 30332 USA (e-mail: logii@qq.com).

Maryam Saeedifard is with the School of Electrical and Computer Engineering, Georgia Institute of Technology, Atlanta, GA 30332 USA (e-mail: maryam@ece.gatech.edu).

Omer C. Onar is with the Electrical and Electronics Systems Research Division, Oak Ridge National Laboratory, Oak Ridge, TN 37831 USA (e-mail: onaroc@ornl.gov).

Qingxin Yang is with the Tianjin University of Technology, Tianjin 300384, China (e-mail: qxyang@tjut.edu.cn).

Changsong Cai is with the School of Electrical Engineering and Automation, Wuhan University, Wuhan 430072, China (e-mail: changsongcai@whu.edu.cn).

Color versions of one or more of the figures in this article are available online at https://ieeexplore.ieee.org.

Digital Object Identifier 10.1109/TPEL.2020.3021591

I. Introduction

OVER the last decade, development of wireless power transfer (WPT) technology for electric vehicle (EV) charging has gained momentum, mostly because of safety and convenience of charging for the end-users [1]–[3]. In the WPT systems, energy is transferred through the mutual inductance (MI) of the magnetically coupled transmitting and receiving coils, whereas the leakage inductance does not contribute to the active power transfer. Since there is a large gap between the transmitting and receiving coils, WPT systems have a relatively large leakage inductance but a smaller MI [4], [5]. To minimize the input VA rating while maximizing the transferred power, the compensation circuits including lumped inductors, and capacitors are needed.

Series- and parallel-based compensation circuits are the most basic circuits that have been widely investigated from the earliest stage [6]–[8]. Compared to these basic circuits, high-order topologies, which offer more degrees of freedom (DoF) in terms of tuning and load independent constant current (CC) or constant voltage (CV) output, are becoming increasely popular [9]–[12]. Nevertheless, high-order topologies inevitably adopt more components, which add to the system volume and cost. Among the additional components adopted in high-order compensation topologies, compensation inductors account for the most part of the system volume and cost [13]. In conventional *LCC* or *LCL* tuned WPT systems, the resonant tuning inductor is a closed magnetic core-based inductor; therefore, it does not contribute to the power transfer. In addition, the conventional magnetic-core-based inductor design at high frequencies and currents is challenging. To exploit the advantages of high-order topologies while minimizing their adverse impacts imposed by adoption of extra inductors, inductor integration design becomes of significant importance.

Zhang [14], Kan [15], [16], and Dang *et al.* [17] provided solutions for inductor integration design of high-order topologies based on bipolar and unipolar coil combinations to decouple the compensation coil from the system. A unipolar coil generates vertical magnetic flux from the center of the coil with only one polarity, while a bipolar coil generates horizontal magnetic flux with two opposite polarities. The bipolar coil can be symmetrically aligned with the unipolar coil such that the magnetic flux coupled between one polarity of the bipolar coil to the unipolar

coil equals to that from the opposite polarity. Consequently, the equivalent net magnetic flux equals zero and the coils become decoupled [16]. By decoupling the compensation coil from the receiving coil, compensation calculation becomes simple and similar to the conventional high-order topologies without any additional couplings. Nevertheless, in the aforementioned inductor integration designs, the compensation coil can be integrated by coil decoupling design, while the magnetic field of the compensation inductor does not make any contribution to power transfer.

To make use of the magnetic field generated by the compensation inductor in circuit integration design, Gao *et al.* [18] coupled two bipolar coils in an *LCL* circuit and achieves input zero phase angle (ZPA) and CV output. The compensation coil is coupled with both the transmitting and receiving coils. However, 90° current phase difference between the integrated coils on the primary side leads to the reactive power flow inside the system, which adds to the system VA rating and power losses [2]. Yan *et al.* [19] used the compensation coil to transfer power to the receiving coil, while the compensation coil is decoupled from the transmitting coil. By bringing in the additional coupling between the compensation and receiving coils, the resonant frequency shifts as the load changes. Regarding high-order topologies, it is desired to use the magnetic field generated by the compensation coil for power transfer to the receiving coil, while preserving the load-independent ZPA and output characteristics. In addition, the reactive power flow between the primary coils due to the integration should be minimized to reduce the input VA rating. However, exploiting the compensation coil to transfer power to the receiving coil creates an additional coupling between them. By using the conventional compensation calculation method under the additional coupling, wherein only the self-inductance values of the inductors are considered, the system will lose its load-independent characteristics, which is the most significant advantage of high-order topologies. Therefore, the additional coupling is considered disadvantageous under the conventional compensation, and specific coil decoupling designs are preferred to enable inductor integration. To achieve inductor integration while making use of the magnetic field generated by the compensation inductor without any specific coil decoupling consideration, there is a need for a new approach to calculate the compensation component sizing considering the extra couplings.

On top of the aforementioned problems in magnetic integration design, imperfect parking alignment, especially misalignment on the horizontal plane, is another practical problem of wireless EV charging as it reduces the mutual coupling compared to the best aligned condition, which results in the decrease of the transmitted power and system efficiency [20]–[22]. Therefore, proper coil design is important [23]–[26] to stabilize the MI under misalignment. Among various coil designs, unipolar is the most frequently adopted one for wireless EV charging due to its simple structure and relatively higher coupling factor. It also features identical misalignment tolerance on both X- and Y-directions. Nonetheless, the magnetic flux coupling between unipolar coils decays rapidly as misalignment increases, which is not an ideal design for misalignment conditions. To improve the unipolar coil misalignment tolerance capability on the entire horizontal plane, a coil design is proposed in [27]. By employing a reversely connected inner coil, the MI between the transmitting and receiving coils can be stabilized to resist the coupling variations. Finite-element analysis (FEA) is used to assess the stability of the equivalent MI of all designs under misalignments. The optimized coil designs with a stable MI within the misalignment tolerant range shows its effectiveness in stabilizing the power transferred to the receiving coil. However, calculation and comparison of all the coil designs under misalignment by the FEA is time consuming [28]. An more efficient optimization algorithm to obtain the inner coil design to stabilize the equivalent MI is needed.

The *LCL-S* circuit is a fundamental and widely-used high-order topology, which features simple structure and, compared to other high-order topologies, is easier to be designed and analyzed. Moreover, it uses the same coils on the primary side, thereby enabling identical coil design to share the ferrite layer. In addition, *LCL-S* circuit can achieve constant current source on primary coil and constant load independent output on the secondary side, which reduces the requirement on cycle to by cycle communications or control between the primary and secondary side. Therefore, the *LCL-S* circuit is used for the integration design in this article. This article attempts to exploit the magnetic field generated by the compensation coil to transfer power to the receiving coil on top of the integration design. To this end, two identical coils are employed and firmly attached to each other to share the same magnetic conduction path. A compensation method is derived to achieve both load-independent input ZPA and CC output, which enables the integration design without any coil decoupling considerations on the primary side in the conventional integration designs. In addition, the proposed compensation method enforces identical currents in terms of the magnitude and the phase angle into the coils on the primary side. Therefore, the transmission field is enhanced while no reactive power exists between the primary coils. For further stabilization of the output power under misalignment, an efficient FEA-based optimization algorithm with less computational effort and trials is developed to improve the coil misalignment tolerance, in which a reversely connected inner coil is employed to achieve a constant equivalent MI within the transmission area. This approach preserves the load-independent features of high-order circuits. Meanwhile, the implementation and the concept of power transfer by the compensation coil is the main distinction from other integration designs.

The rest of this article is organized as follows. In Section II, the proposed system configuration and its equivalent models are analyzed and the compensation method to achieve input ZPA, CC output, and field enhancement is derived. The proposed design is also analytically compared with the conventional *LCC-S* and the *LCC-LCC* circuits. Section III presents the misalignment tolerant coil design and the optimization strategy. Section IV expands the FEA results of the proposed design with more standard design cases and makes a comparison. Experimental results for both the proposed design and the conventional *LCC-LCC* system with identical nominal outputs are provided and compared in Section V. Finally, Section VI concludes this article.

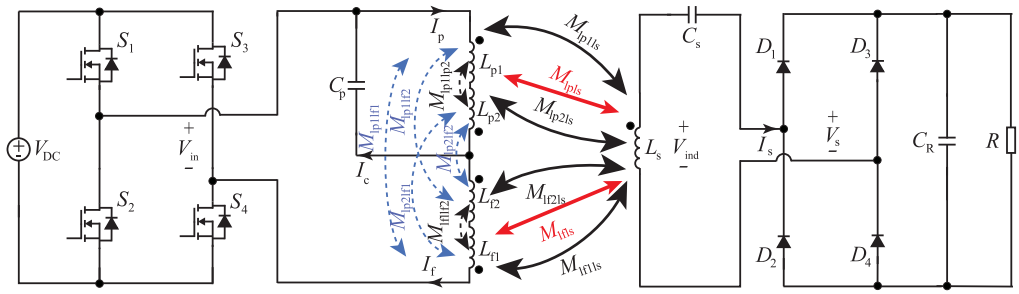

Fig. 1. Proposed field enhancement integration circuitry design based on the *LCL-S* topology. $V_{\rm dc}$ is the input dc voltage. S_1–S_4 and D_1–D_4 are the switches and diodes of the inverter and rectifer, respectively. $L_{\rm p1}$ and $L_{\rm p2}$ constitute the transmitting coils, while $L_{\rm f1}$, $L_{\rm f2}$ are the compensation inductors. $L_{\rm s}$ is the inductance of the receiving coil. The MIs are referred to with the notation of $M_{1(x)1(y)}$, where $x = \{\rm f1, f2, p1, p2\}$, $y = \{\rm f1, f2, p1, p2, s\}$, and M describes the mutual coupling between L_x and L_y. $V_{\rm in}$ and $V_{\rm s}$ are the output voltage of the inverter and the input voltage of the diode-bridge rectifier, respectively. $C_{\rm p}$ and $C_{\rm s}$ are the capacitors to compensate the inductive components of the respective resonant networks on the primary and secondary sides, respectively. $C_{\rm R}$ and R are the filtering capacitor and load resistance, respectively. $V_{\rm ind}$ is the induced voltage on $L_{\rm s}$. $I_{\rm f}$, $I_{\rm p}$, and $I_{\rm s}$ are the currents of corresponding branches on the primary and secondary sides.

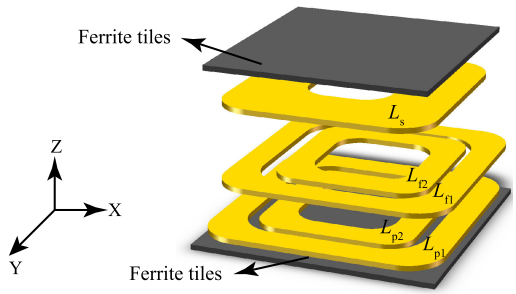

Fig. 2. Exploded view of the coil arrangement featuring field enhancement.

II. System Configuration and Design

A. System Configuration and Misalignment Tolerance Analysis

The configuration of the proposed WPT system, which is based on the *LCL-S* compensation topology, is shown in Fig. 1. The system of Fig. 1 features a high DoF in terms of tuning compared to series- or parallel-based compensation circuits [11]. The full-bridge inverter on the primary side, converts $V_{\rm dc}$ to an ac voltage $V_{\rm in}$, with the nominal operation frequency of 85 kHz, which is within the standard operating frequency range of wireless EV charging, according to SAE J2954 [29].

($L_{\rm p1}$, $L_{\rm p2}$) and ($L_{\rm f1}$, $L_{\rm f2}$) are two pairs of coils reversely connected on the primary side to form the misalignment tolerant coils. The details of the coils arrangements and the coil misalignment tolerance principles will be discussed later in Fig. 2 and (1), respectively. The compensation and transmitting coils are identical for ease of integration.

Since there is no wired connection between the primary and secondary sides, the high-frequency ac power is transmitted wirelessly through the main MIs: $M_{\rm lp1ls}$, $M_{\rm lp2ls}$, $M_{\rm lf1ls}$, and $M_{\rm lf2ls}$, which are represented by the arrows with black solid line in Fig. 1. To simplify the analysis, the equivalent main MIs are defined as $M_{\rm lfls} = M_{\rm lf2ls} - M_{\rm lf1ls}$ and $M_{\rm lpls} = M_{\rm lp2ls} - M_{\rm lp1ls}$, which are the arrows with red solid line in Fig. 1.

To make the WPT system more compact, the compensation coils $L_{\rm f1}$ and $L_{\rm f2}$ are integrated into the main coils $L_{\rm p1}$ and $L_{\rm p2}$. As a result, additional couplings appear among the compensation and transmitting coils on the primary side, which are represented by $M_{\rm lp1lf1}$, $M_{\rm lp2lf1}$, $M_{\rm lp1lf2}$, and $M_{\rm lp2lf2}$, plotted as the blue dashed lines in Fig. 1. In the existing work on inductor integration design of WPT in [15]–[17], the compensation coils are designed to be decoupled from the transmitting coils and the magnetic field generated by the compensation coils does not contribute to the transmission capacity. However, in the proposed design, in this article, ($L_{\rm p1}$, $L_{\rm p2}$) and ($L_{\rm f1}$, $L_{\rm f2}$) are closely overlapped and share the same magnetic flux path such that the mutual couplings among the two layers of coils are sufficiently strong, and are not neglected when calculating the compensation capacitor.

To illustrate the integrated coil design, the exploded view of the coils arrangement is provided in Fig. 2. It should be noted that, under an ideal case, ($L_{\rm p1}$, $L_{\rm p2}$) and ($L_{\rm f1}$, $L_{\rm f2}$) can alternate the arrangements to be one on top of the other as the coils are identical. In this article, ($L_{\rm f1}$, $L_{\rm f2}$) are stacked closely to the top of ($L_{\rm p1}$, $L_{\rm p2}$) as the compensation coils as an example. The ferrite tiles are attached to the bottom of ($L_{\rm p1}$, $L_{\rm p2}$) for magnetic shielding. A unipolar coil $L_{\rm s}$ is attached to the top ferrite tiles as the receiving coil. The distance between ($L_{\rm f1}$, $L_{\rm f2}$) and $L_{\rm s}$ is equal to $d = 150$ mm, which is a typical ground clearance level for most of the midsize sedan electric vehicles, when they are center aligned.

In Fig. 1, $C_{\rm p}$ is used to tune the primary-side network to resonate while suppressing the circulating current caused by the overlapped coils structure. Since the mutual couplings among the primary coils are complex, for the sake of simplicity, assume that $L_{\rm p} = L_{\rm p1} + L_{\rm p2} - 2M_{\rm lp1lp2}$ and $L_{\rm f} = L_{\rm f1} + L_{\rm f2} - 2M_{\rm lf1lf2}$. By defining $M_{\rm lf} = M_{\rm lp1lf2} + M_{\rm lp2lf1} - M_{\rm lp1lf1} - M_{\rm lp2lf2}$, the compensation topology in Fig. 1 can be decoupled to Fig. 3(a) using the "M model"

$$\begin{aligned} V_{\rm ind} &= j\omega(M_{\rm lf2ls} - M_{\rm lf1ls})I_{\rm f} - j\omega(M_{\rm lp2ls} - M_{\rm lp1ls})I_{\rm p} \\ &= j\omega M_{\rm lfls} I_{\rm f} - j\omega M_{\rm lpls} I_{\rm p}. \end{aligned} \tag{1}$$

The power is transferred from the primary to the receiving side through the mutual couplings based on (1), where the voltage induced on $L_{\rm s}$ is defined as $V_{\rm ind}$. It should be noted that first harmonic approximation is used in the following analysis of the network compensation characteristics [12], [30]. While $M_{\rm lf1ls}$, $M_{\rm lf2ls}$, $M_{\rm lp1ls}$, and $M_{\rm lp2ls}$ inevitably decrease as the misalignment increase, if the decrease in $M_{\rm lf1ls}$ and $M_{\rm lf2ls}$ are

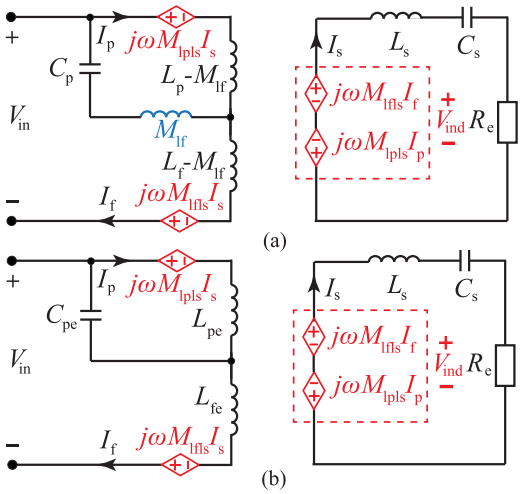

Fig. 3. Equivalent model representing the mutual couplings among the coils. (a) $M_{\rm lf}$ decoupled circuit. (b) Simplified circuit considering $M_{\rm lf}$ on the branches of the primary side.

the same within the range of misalignment tolerant design, $M_{\rm lf2ls} - {\rm M}_{\rm lf1ls}$ stay constant under any given position within the range [27]. The same theory applies to $M_{\rm lp1ls}$ and $M_{\rm lp2ls}$ in achieving a constant $M_{\rm lpls}$. Consequently, $V_{\rm s}$ as the ac input voltage of the diode-bridge rectifier, will not change as misalignment increases by (1).

To simplify the analysis, the equivalent circuit on the primary side, by decoupling $M_{\rm lf}$, can be simplified to the circuit shown in Fig. 3(a). By combining $M_{\rm lf}$ with the components on corresponding branches, Fig. 3(a) can be further simplified to Fig. 3(b)

$$L_{\rm pe} = L_{\rm p} - M_{\rm lf} \tag{2}$$

$$L_{\rm fe} = L_{\rm f} - M_{\rm lf} \tag{3}$$

$$\frac{1}{j\omega C_{\rm pe}} = j\omega M_{\rm lf} + \frac{1}{j\omega C_{\rm p}} \tag{4}$$

$$R_{\rm e} = \frac{8}{\pi^2} R \tag{5}$$

$$V_{\rm in} = \frac{2\sqrt{2}}{\pi} V_{\rm dc}. \tag{6}$$

Based on Fig. 3(b), the WPT system in Fig. 1 can be modeled by

$$\begin{bmatrix} j\omega L_{\rm fe} + \frac{1}{j\omega C_{\rm pe}} & -\frac{1}{j\omega C_{\rm pe}} & -j\omega M_{\rm lfls} \\ -\frac{1}{j\omega C_{\rm pe}} & j\omega L_{\rm pe} + \frac{1}{j\omega C_{\rm pe}} & j\omega M_{\rm lpls} \\ -j\omega M_{\rm lfls} & j\omega M_{\rm lpls} & Z \end{bmatrix} \begin{bmatrix} I_{\rm f} \\ I_{\rm p} \\ I_{\rm s} \end{bmatrix} = \begin{bmatrix} V_{\rm in} \\ 0 \\ 0 \end{bmatrix} \tag{7}$$

in which

$$Z = j\omega L_{\rm s} + \frac{1}{j\omega C_{\rm s}} + R_{\rm e}. \tag{8}$$

Under ideal tuning, i.e., $C_{\rm s} = \frac{1}{\omega^2 L_{\rm s}}$, and when the load R is assumed to be constant for simplification, Z becomes purely resistive and stays unchanged. Based on (7), as long as $M_{\rm lpls}$ and $M_{\rm lfls}$ are constant, (7) is immune to misalignment and the output characteristics of the circuit remains unchanged.

Based on the aforementioned analysis, the primary goals of the system design are as follows:

1) integrate the compensation inductor of the circuit into the charging pad design while preserving its load-independent output characteristic;
2) exploit the magnetic field of the compensation coil to enhance the power transmission capacity;
3) improve misalignment tolerance performance by a stable equivalent MI coil design.

B. Integration Design and Compensation Analysis

The primary objective of the integration design is to integrate the compensation inductors into the charging pad while exploring the possibility of extending the power transmission capability by using the extra magnetic field generated by the compensation coils. Since two layers of coils are firmly attached to each other and share the same magnetic flux conduction path, the magnetic fields generated by both layers contribute to the transmission field.

To enhance the transmission field, the current flow in both coil pairs should be in phase. Otherwise, the magnetic fields generated by unequal phase in each branch will induce reactive power flow in the circuit and increase the current stress of the semiconductor devices, which translates to higher power losses. In addition, considering the identical coil pairs used in the design, the ideal case is that the magnitudes of the current in both coil pairs to be identical, such that both coils transfer the same amount of power to the receiving side. This is the best case to synchronize the coil parameters regarding its design, fabrication, aging process, and reliability/maintenance in practice. Similar approaches are provided in [31], where the current magnitudes of two decoupled coils are controlled to be identical to transfer power due to the same consideration. Taking these factors into account, the best operation case to be solved, can be interpreted as $I_{\rm p} = -I_{\rm f}$. Furthermore, to minimize the system VA rating, ZPA is intended for compensation capacitor calculation. Based on these considerations, the primary requirements for the compensation calculation can be summarized as follows.

1) The equivalent impedance observed from the output of the inverter should be purely resistive.
2) The magnetic fields generated by $L_{\rm f}$ and $L_{\rm p}$ should be identical both in phase and magnitude.

This article analyzes only ZPA realization by compensation calculation. Soft-switching operation can be achieved by ZPA calculation and ZVS realization [11], [32], and is not discussed as it is not the scope of this article.

Considering the compensation strategy to meet the aforementioned requirements, the current $I_{\rm f}$, $I_{\rm p}$, and $I_{\rm s}$ in each branch of Fig. 1 can be derived by

$$I_{\rm f} = \frac{(\omega^2 C_{\rm pe} L_{\rm pe} Z - j\omega^3 M_{\rm lpls}^2 C_{\rm pe} - Z) V_{\rm in}}{\tau} \tag{9a}$$

$$I_{\rm p} = -\frac{(j\omega^3 M_{\rm lpls} M_{\rm lfls} C_{\rm pe} + Z) V_{\rm in}}{\tau} \tag{9b}$$

$$I_{\rm s} = \frac{j(\omega^3 M_{\rm lfls} C_{\rm pe} L_{\rm pe} - \omega M_{\rm lfls} + \omega M_{\rm lpls}) V_{\rm in}}{\tau} \tag{9c}$$

where τ is expressed by

$$\tau = \omega(\omega^3 C_{\rm pe}(L_{\rm fe}M_{\rm lpls}^2 + L_{\rm pe}M_{\rm lfls}^2) - (M_{\rm lfls} - M_{\rm lpls})^2) + jZ(\omega^2 C_{\rm pe}L_{\rm fe}L_{\rm pe} - L_{\rm fe} - L_{\rm pe}). \quad (10)$$

Each current component can be expressed in the form of $I_n = a_n + b_n i$, where the subscript n represents the corresponding index of each branch, while a and b refer to the real and imaginary parts of the current, respectively. For compensation analysis and to simplify the equations, it is assumed that the inductances and MIs of the two coils are identical, as both layers are identical and firmly attached. Consequently, $L_{\rm f} = L_{\rm p}$, $M_{\rm lfls} = M_{\rm lpls}$ and the complex form of $L_{\rm f}$ and $L_{\rm p}$ can be decomposed into (11), as shown at the bottom of this page.

Based on (11), under any compensation condition, $\frac{a_{\rm p}}{a_{\rm f}} = -1$, such that the first requirement converts to $b_{\rm f} = 0$. Therefore, by making $b_{\rm f} = 0$, the solutions to the compensation capacitor $C_{\rm pe}$ are derived as

$$C_{\rm pe1} = \frac{3L_{\rm pe}^2 + \sqrt{\Delta_2 + L_{\rm pe}^4}}{\omega^2(\Delta_1 + 2L_{\rm pe}^3)} \quad (12a)$$

$$C_{\rm pe2} = \frac{3L_{\rm pe}^2 - \sqrt{\Delta_2 + L_{\rm pe}^4}}{\omega^2(\Delta_1 + 2L_{\rm pe}^3)} \quad (12b)$$

where

$$\Delta_1 = \frac{4\omega^2 M_{\rm lpls}^4 L_{\rm pe}}{Z^2} \quad (13a)$$

$$\Delta_2 = \frac{-16\omega^2 M_{\rm lpls}^4 L_{\rm pe}^2}{Z^2}. \quad (13b)$$

To further simplify (12), Δ_1 and Δ_2 are compared with $2L_{\rm pe}^3$ and $L_{\rm pe}^4$, respectively, which are the two terms in $\omega^2(\Delta_1 + 2L_{\rm pe}^3)$ and $(\Delta_2 + L_{\rm pe}^4)$ in (12). The weight ratios of Δ_1 and Δ_2 over the other components in the corresponding terms can be expressed as

$$\left|\frac{\Delta_1}{2L_{\rm pe}^3}\right| = \frac{2\omega^2 M_{\rm lpls}^4}{Z^2 L_{\rm pe}^2} \quad (14a)$$

$$\left|\frac{\Delta_2}{L_{\rm pe}^4}\right| = \frac{16\omega^2 M_{\rm lpls}^4}{Z^2 L_{\rm pe}^2} = 8\left|\frac{\Delta_1}{2L_{\rm pe}^3}\right| < 3\%. \quad (14b)$$

To estimate the values of (14), $M_{\rm lpls}$ is typically designed below $0.05L_{\rm pe}$ [27] and the system is ideally compensated while R is selected to be around 10-50 Ω for EV charging [33], [34]. By adopting the parameters in the experiment in Section V as an example to verify the estimation, the ratio derived from (14b) is less than 3% and it can be observed that the value of (14b) is 8 times of the value of (14a). As a result, $2L_{\rm pe}^3$ and $L^4{}_{\rm pe}$ are the dominant components in $\omega^2(\Delta_1 + 2L_{\rm pe}^3)$ and $(\Delta_2 + L^4{}_{\rm pe})$, respectively. Since Δ_1 and Δ_2 in (12) are sufficiently small and can be neglected, (12) can be simplified to

$$C_{\rm pe1} = \frac{3L_{\rm pe}^2 + \sqrt{L_{\rm pe}^4}}{2\omega^2 L_{\rm pe}^3} = \frac{2}{\omega^2 L_{\rm pe}} \quad (15a)$$

$$C_{\rm pe2} = \frac{3L_{\rm pe}^2 - \sqrt{L_{\rm pe}^4}}{2\omega^2 L_{\rm pe}^3} = \frac{1}{\omega^2 L_{\rm pe}}. \quad (15b)$$

Both $C_{\rm pe1}$ and $C_{\rm pe2}$ meet the first compensation requirement. The second requirement is met when $b_{\rm p} = b_{\rm f} = 0$. As both $C_{\rm pe1}$ and $C_{\rm pe2}$ make $a_{\rm f} = -a_{\rm p}$ and $b_{\rm f} = 0$, $b_{\rm p}$ should be calculated to evaluate the compensation results of both capacitors. Ideally, $b_{\rm p}$ equals zero to achieve a perfect field enhancement without any circulating current. However, due to complex coupling and imperfections, it is not possible for $b_{\rm p}$ to become zero. To minimize the phase difference between $I_{\rm f}$ and $I_{\rm p}$, $b_{\rm p}$ should be as close as possible to zero. Subsequently, both real and imaginary components of current in $L_{\rm f}$ and $L_{\rm p}$ are calculated to compare the compensation results of $C_{\rm pe1}$ and $C_{\rm pe2}$.

To identify the current components with respect to each $C_{\rm pe}$ compensation, $a_{n\_{\rm cpe}k}$ and $b_{n\_{\rm cpe}k}$ are used to indicate the real and imaginary parts of the current in each branch under different $C_{\rm pe}$, where $n = \{f, p\}$ and $k = \{1, 2\}$

$$a_{\rm f\_cpe1} = -a_{\rm p\_cpe1} = \frac{R_{\rm e}V_{\rm in}}{4\omega^2 M_{\rm lpls}^2} \quad (16a)$$

$$b_{\rm f\_cpe1} = 0, b_{\rm p\_cpe1} = -\frac{V_{\rm in}}{2\omega L_{\rm pe}} \quad (16b)$$

$$a_{\rm f\_cpe2} = -a_{\rm p\_cpe2} = \frac{M_{\rm lpls}^2 R_{\rm e}V_{\rm in}}{4\omega^2 M_{\rm lpls}^4 + L_{\rm pe}^2 R^2{}_{\rm e}} \quad (16c)$$

$$b_{\rm f\_cpe2} = 0, b_{\rm p\_cpe2} = -\frac{(2\omega^2 M_{\rm lpls}^4 + L_{\rm pe}^2 R_{\rm e}^2)V_{\rm in}}{\omega L_{\rm pe}(4\omega^2 M_{\rm lpls}^4 + L_{\rm pe}^2 R^2)}. \quad (16d)$$

To quantitatively evaluate and compare the degree of $b_{\rm p}$ over $a_{\rm p}$, δ_1 and δ_2 are defined as ratios of the imaginary part over the real part of the current under the compensation condition of

$$a_{\rm f} = \frac{\omega^4 M_{\rm lpls}^2 C_{\rm pe}^2 Z V_{\rm in}}{4\omega^6 M_{\rm lpls}^4 C_{\rm pe}^2 + (\omega^2 L_{\rm pe}C_{\rm pe}Z - 2Z)^2} \quad (11a)$$

$$a_{\rm p} = -\frac{\omega^4 M_{\rm lpls}^2 C_{\rm pe}^2 Z V_{\rm in}}{4\omega^6 M_{\rm lpls}^4 C_{\rm pe}^2 + (\omega^2 L_{\rm pe}C_{\rm pe}Z - 2Z)^2} \quad (11b)$$

$$b_{\rm f} = -\frac{(2\omega^6 M_{\rm lpls}^4 C_{\rm pe}^2 Z + \omega^4 L_{\rm pe}^2 C_{\rm pe}^2 Z^2 - 3\omega^2 L_{\rm pe}C_{\rm pe}Z^2 + 2Z^2)V_{\rm in}}{\omega L_{\rm pe}(4\omega^6 M_{\rm lpls}^4 C_{\rm pe}^2 + (\omega^2 L_{\rm pe}C_{\rm pe}Z - 2Z)^2)} \quad (11c)$$

$$b_{\rm p} = \frac{(-2\omega^6 M_{\rm lpls}^4 C_{\rm pe}^2 Z + \omega^2 L_{\rm pe}C_{\rm pe}Z^2 - 2Z^2)V_{\rm in}}{\omega L_{\rm pe}(4\omega^6 M_{\rm lpls}^4 C_{\rm pe}^2 + (\omega^2 L_{\rm pe}C_{\rm pe}Z - 2Z)^2)} \quad (11d)$$

TABLE I
COMPARISON OF THE NUMBERS OF PROBLEMS TO BE CALCULATED UNDER EACH D_k USING THE CONVENTIONAL AND PROPOSED METHODS

Inner coil outer dimension	Numbers of problems to be solved	
	Conventional method	Proposed method
D_1	25	10
D_2	24	9
D_3	23	9
D_4	22	8
D_5	21	7
D_6	20	7
D_7	19	6
D_8	18	6
D_9-D_{25}	153	0
Numbers in total	325	62

C_{pe1} and C_{pe2}, respectively. Under the nominal frequency of 85 kHz, δ_1 and δ_2 are

$$\delta_1 = \left|\frac{b_{\mathrm{p\_cpe1}}}{a_{\mathrm{p\_cpe1}}}\right| = \frac{2\omega M_{\mathrm{lpls}}^2}{L_{\mathrm{pe}} R_{\mathrm{e}}} \approx 0 \tag{17a}$$

$$\delta_2 = \left|\frac{b_{\mathrm{p\_cpe2}}}{a_{\mathrm{p\_cpe2}}}\right| = \frac{2\omega^2 M_{\mathrm{lpls}}^4 + L_{\mathrm{pe}}^2 R^2{}_{\mathrm{e}}}{\omega M_{\mathrm{lpls}}^2 L_{\mathrm{pe}} R_{\mathrm{e}}} \tag{17b}$$

$$\frac{\delta_1}{\delta_2} = \frac{2\omega^2 M_{\mathrm{lpls}}^4}{2\omega^2 M_{\mathrm{lpls}}^4 + L_{\mathrm{pe}}^2 R^2{}_{\mathrm{e}}} > 0.015. \tag{17c}$$

Based on the analysis of the relationships between M_{lpls}, L_{pe}, and Z discussed in (14), it can be observed from (17) that under C_{pe1} compensation, $b_{\mathrm{p\_cpe1}}$ is a small fraction compared to $a_{\mathrm{p\_cpe1}}$ such that δ_1 is close to 0. This means that the imaginary part of I_{p} can be ignored and only real power exists in L_{p}. If C_{pe2} is adopted in the circuit, the magnitude of $b_{\mathrm{p\_cpe2}}$ becomes comparable to the magnitude of $a_{\mathrm{p\_cpe2}}$. This means that a sensible phase difference exists between I_{f} and I_{p} under C_{pe2} and the device current stress, due to magnetic field cancellation on the primary side, would increase. The ratio of δ_1 over δ_2 in (17c) also confirms that the percentage of imaginary part of current under C_{pe1} compensation compared to that of C_{pe2} compensation is negligible. To verify how the load variations impact δ_1 and δ_2, the parameters from Table II are used as an example to calculate and plot (17a) and (17b) in Fig. 4(a). The operating frequency band is swept from 70 kHz to 100 kHz, while the load resistance R changes from 30 Ω to 100 Ω with a step size of 10 Ω. R_{e} in (17) can be calculated using R from (5). It can be observed that δ_1 reaches 0 at 85 kHz while δ_2 reaches 0 at 89.1 kHz, which is far from the desired operating frequency. The frequency at which $\delta_1 = 0$ does not change as load varies.

The current gains of the proposed design under the compensation of C_{pe1} and C_{pe2} within the same frequency band are also compared in Fig. 4(b) by using the same parameters from Table II. Both capacitor values achieve CC output at a specific frequency, where C_{pe1} reaches CC at 85 kHz while C_{pe2} achieves CC at 89.1 kHz.

It can be observed from Fig. 4 that the system achieves similar outputs under C_{pe1} and C_{pe2} regarding their corresponding resonant frequencies. As the nominal operation frequency of this article is 85 kHz, C_{pe2} is not suitable for compensation and is ignored. The compensation capacitor C_{p} can be derived based on C_{pe1} by using (2) and (4), with the compensation conditions

TABLE II
PARAMETERS OF THE EXPERIMENTAL PROTOTYPE

Symbol	Description	Value
V_{dc}	DC input voltage	65 V
P	Rated power	1 kW
d	Nominal gap distance between pads	150 mm
T	X-axis and Y-axis misalignment tolerance	200 mm
f	Switching frequency	85.00 kHz
L_{f}	Compensation coil inductance	83.12 μH
L_{p}	Transmitting coil inductance	96.14 μH
L_{s}	Receiving coil inductance	216.04 μH
M_{lf}	MI between the compensation and transmitting coils	76.61 μH
M_{eq}	Nominal equivalent MI	10.77 μH
R	Load resistance	40 Ω
C_{p}	Capacitor on the primary side	43.41 nF
C_1	Compensation capacitor for the inductance error of the transmitting coil	332.79 nF
C_{s}	Capacitor on the receiving side	16.21 nF
a_{o}	Transmitting coil outside dimension	450 mm × 450 mm × 3 mm
a_{i}	Inner coil inside dimension	300 mm × 300 mm × 3 mm
a_{r}	Receiving coil outside dimension	400 mm × 400 mm × 3 mm
σ	Initial permeability of ferrite TDK PC90	2200
ϕ	Litz wire	AWG38 × 420 × 2

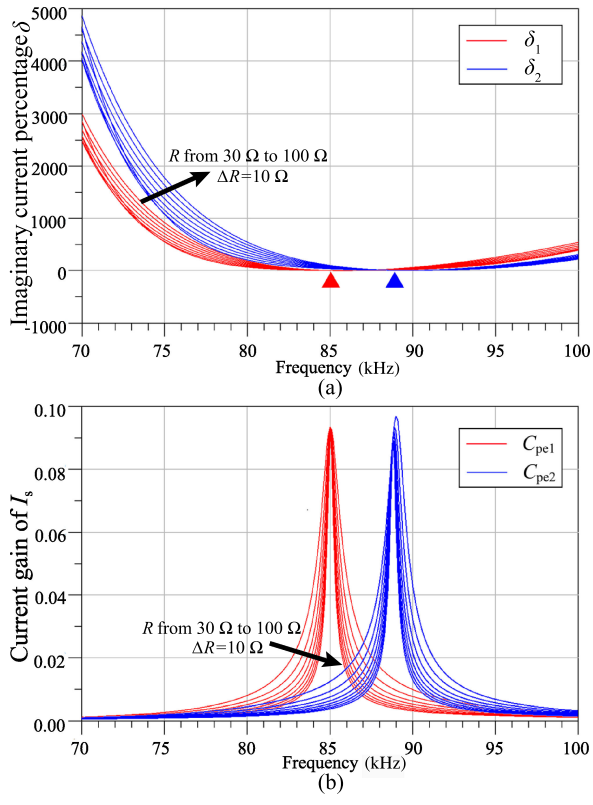

Fig. 4. Analytical results of I_{p} and I_{s} under the compensation of C_{pe1} and C_{pe2}. (a) Imaginary current percentage δ. (b) Current gain of I_{s}.

concluded as

$$C_{\mathrm{p}} = \frac{2}{\omega^2(L_{\mathrm{p}} + M_{\mathrm{lf}})} \tag{18a}$$

$$C_{\mathrm{s}} = \frac{1}{\omega^2 L_{\mathrm{s}}}. \tag{18b}$$

Even though the proposed integration design is based on the conventional *LCL-S* compensation circuit, the new design shows different characteristics under the proposed compensation method. The conventional *LCL-S* compensation circuit, under ideal tuning, is load independent and the circuit operates as a CV source. The proposed design also offers a load independent output while it operates as a CC source, which is similar to the double-sided *LCC* circuit. Therefore, the current gain versus the inverter output voltage of the proposed design is derived and compared with both the conventional *LCL-S* and double-sided *LCC* circuits, which also provides a CC output, as in (19) [12], [32]. To make a fair comparison, the transmitting and receiving coils in all systems are the same and each system is tuned to its ideal operating status

$$G_{\mathrm{V\_LCL}} = \left|\frac{V_{\mathrm{out}}}{V_{\mathrm{in}}}\right| = \left|-\frac{M_{\mathrm{lpls}}}{L_{\mathrm{p}}}\right| \tag{19a}$$

$$G_{\mathrm{V\_LCC}} = \left|\frac{I_{\mathrm{out}}}{V_{\mathrm{in}}}\right| = \left|\frac{jM_{\mathrm{lpls}}}{\omega L_{\mathrm{f1}} L_{\mathrm{f2}}}\right| \tag{19b}$$

$$G_{\mathrm{C\_int}} = \left|\frac{I_{\mathrm{s}}}{V_{\mathrm{in}}}\right| = \left|\frac{j}{2\omega M_{\mathrm{lpls}}}\right| \tag{19c}$$

where the subscripts "*LCL*," "*LCC*," and "int" represent the conventional *LCL-S* circuit, double-sided *LCC* circuit, and the proposed integrated design, respectively.

The output power is also derived and compared with the conventional *LCL-S* and double-sided *LCC* circuits, and the results are as following [12], [32]:

$$P_{\mathrm{out\_}LCL} = \frac{M_{\mathrm{lpls}}^2 V_{\mathrm{in}}^2}{L_{\mathrm{p}}^2 R_{\mathrm{e}}} \tag{20a}$$

$$P_{\mathrm{out\_}LCC} = \frac{M_{\mathrm{lpls}}^2 V_{\mathrm{in}}^2 R_{\mathrm{e}}}{\omega^2 L_{\mathrm{f1}}^2 L_{\mathrm{f2}}^2} \tag{20b}$$

$$P_{\mathrm{out\_int}} = \frac{V_{\mathrm{in}}^2 R_{\mathrm{e}}}{4\omega^2 M_{\mathrm{lpls}}^2} \tag{20c}$$

$$\gamma_1 = \frac{P_{\mathrm{out\_int}}}{P_{\mathrm{out\_}LCL}} = \frac{L_{\mathrm{p}}^2 R_{\mathrm{e}}^2}{4\omega^2 M_{\mathrm{lpls}}^4} \gg 1 \tag{20d}$$

$$\gamma_2 = \frac{P_{\mathrm{out\_int}}}{P_{\mathrm{out\_}LCC}} = \frac{L_{\mathrm{f1}}^2 L_{\mathrm{f2}}^2}{4M_{\mathrm{lpls}}^4} \tag{20e}$$

where γ_1 and γ_2 are the ratios of the output power of the proposed integrated system over the conventional *LCL-S* and double-sided *LCC* circuits, respectively. As M_{lpls} lies in the denominator of (20c), the output power increases if M_{lpls} decreases, which is also the case in some CC output circuits with voltage source input. However, for the analysis of the circuit under normal operation where M_{lpls} does not equal to zero, (20) should be used. When the receiving coil is absent from the system and M_{lpls} equals zero, the circuit schematic changes and I_{f} becomes limited by the resistances of the L_{f} and L_{p}, which is not the designed situation in this article and is not discussed.

As M_{lpls} is lower than L_{p} or L_{s}, based on (20), γ_1 is much larger than 1 while γ_2 can be adjusted to be around 1. This indicates that the power transmission capacity of the proposed design compared to the conventional *LCL-S* circuit, is increased and is comparable to the double-sided *LCC* circuit.

III. Misalignment Tolerant Coil Design and Optimization

Since due to imperfect parking, misalignment can be random, a symmetrical coil design is preferred to get identical misalignment tolerant capabilities on both *X*- and *Y*-axes. Especially, when rotational misalignment happens, identical misalignment tolerant capabilities on both axes simplify the analysis and design.

As the design is targeted for wireless EV charging, certain dimension restrictions apply to the coil design and transmission distance between the transmitting and receiving coils. The design goal of this section is to improve the misalignment tolerant capability of any given transmitting and receiving coils by adding an optimized inner coil. The transmitting and receiving coil designs are determined according to the system power level and corresponding recommendations in the SAE J2954 [29]. Only the inner coil, which helps the system to achieve a stable equivalent MI, is not determined yet.

It should be noted that the coils are all lumped coils in this article. Unlike the coil designs to improve the coupling or magnetic field uniformity without changing the self-inductance in [35] and [36], the self-inductance of the lumped transmitting coil with an inner coil in series in this article can be higher than the same transmitting coil without an inner coil. Under the same current excitation, a higher self-inductance imposes a higher voltage across the terminals of the transmitting coil, therefore, increases the voltage stress on the compensation capacitor C_{p} in Fig. 1 [31]. To reduce the self-inductance of the misalignment tolerant coil within a given dimension, the number of turns of the coil should be reduced. In addition, the coils on the primary side are double-layered and, thus, the thickness of the laminated coils are increased.

Based on the abovementioned analysis, using parallel windings is a potential solution to reduce the inductance values of the lumped transmitting and receiving coils without changing coil dimensions. The cross-sectional view of the overlapped coil structure using parallel winding is provided in Fig. 5(c). Two parallel Litz-wires are wound from inside to outside. The wires are wound without any gap between the adjacent turns to make the lumped coil. ϕ and D_k are the inner and outer dimensions of the inner coil, respectively.

Taking the current conduction requirement into account, the parallel winding uses Litz-wire, each with a nominal outside diameter of $a = 3$ mm consisting of AWG 38 wires [37]. The coils on the primary side are labeled with their relative current directions in Fig. 5(a) to illustrate the reverse connection of the outer and inner coils.

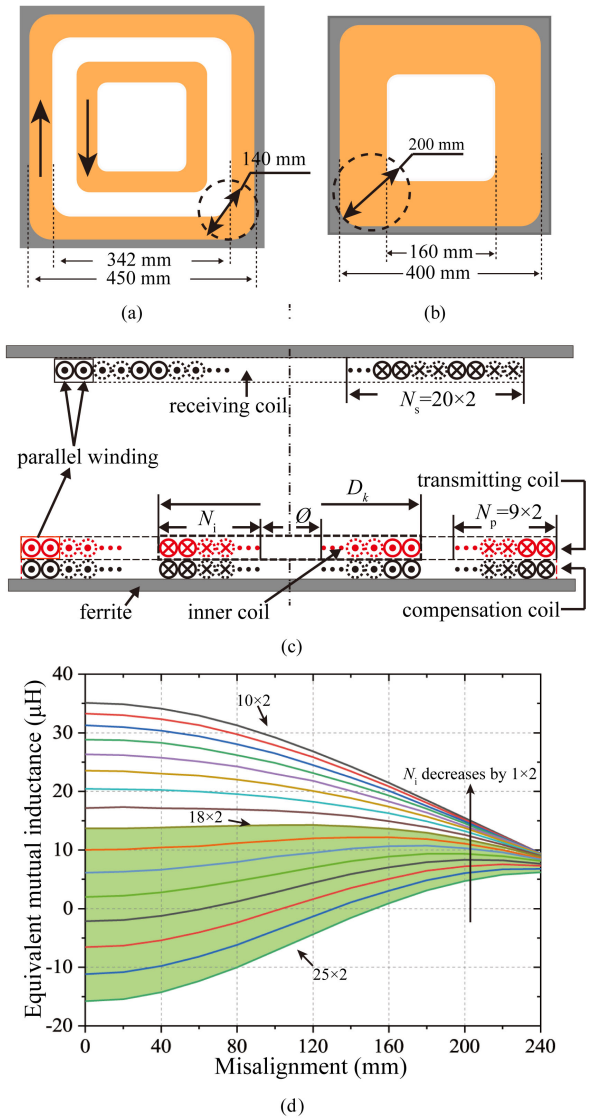

Fig. 5. Coil structure illustration and an example of the conventional optimization. (a) Coils on the primary side. (b) Coil on the secondary side. (c) Cross-sectional view of the overlapped coil structure. (d) Equivalent MI values under misalignment as N_i reduces from 25×2 to 10×2 with a step size of 1×2 when $\phi = 40$ mm.

Since the compensation coil is identical to the transmitting coil, and both are firmly attached to each other, the equivalent M_{eq} is defined to be $M_{eq} = M_{lpls} = M_{lfls}$. Only M_{lpls} is analyzed for simplification.

To achieve a stable M_{eq} and M_{lp2ls} should be well designed to have the same decline of M_{lp1ls} within the misalignment tolerant range according to (4) [27]. As M_{lp1ls} can be determined according to the vehicle design, M_{eq} is expressed by substituting Neumann's formula [38] into M_{lp2ls} as follows:

$$M_{eq} = M_{lp1ls} - M_{lp2ls} = M_{lp1ls} - w\sum_{1}^{N_i}\sum_{1}^{N_s}\left(\frac{\mu_0}{4\pi}\oint_{l_{p2}}\oint_{l_s}\frac{dl_s dl_{p2}}{d_1}\right) \quad (21)$$

where N_i and N_s are the numbers of turns of the inner and receiving coils, respectively. dl_{p2} and dl_s are the current integral elements on the inner and receiving coils, respectively. d_1 represents the distance between dl_{p2} and dl_s.

In this article, the transmitting and receiving coils are both square shaped, and the outer length of the transmitting coil is 450 mm with a number of turns of $N_p = 9 \times 2$, where $(\times 2)$ indicates the parallel winding arrangement and so does the following contents, according to the design recommendations in SAE J2954 [29]. To keep the consistency of the wire and the fabrication method used for the coils, parallel windings are also used for the receiving coil fabrication. The outer length of the receiving coil is 400 mm with $N_s = 20 \times 2$ turns. TDK PC90 ferrite tiles with an initial permeability of 2200 and a thickness of 3 mm are adopted to form the ferrite layers. The distance d between the top of the compensation and the bottom of the receiving coil is 150 mm when they are center aligned.

To obtain a stable equivalent MI by employing an inner coil, Hui [4] used an inner circular coil and builds FEA models with the conventional algorithm for all possible design combinations. However, the conventional optimization method is time consuming as all possible designs need to be calculated. In particular, when misalignment occurs, new meshes have to be regenerated and each remeshed model has to be calculated as a new problem [28]. To better explain the conventional method, the optimization process considering all possible designs can be summarized as follows.

1) Maintain ϕ at its minimum allowed dimension and reduce N_i from its maximum to 0. The maximum N_i is calculated by $(D_{max} - \phi)/(2 \times 2 \times a)$, where D_{max} is the maximum outer dimension of the inner coil. Calculate M_{eq} of each N_i under each misalignment position.
2) Expand the inner coil from inside such that ϕ is increased by a step size of $2 \times 2 \times a$ mm. Update the maximum allowed N_i and reduce N_i from its current maximum to 0, and calculate M_{eq} under each misalignment position.
3) Repeat step 2 till ϕ reaches D_{max}, all combinations can be calculated. Compare all the results and select the coil with the most stable equivalent MI under misalignment as the desired design.

In this article, according to the bending radius requirement of the wires, the minimum allowed dimension of the inner coil is $\phi = 40$ mm. D_{max} is set to be 340 mm since the inner length of the transmitting coil is 342 mm and, thus, the maximum number of turns of the inner coil for optimization is $N_i = 25 \times 2$. By using the conventional optimization method, the number of problems to be solved, i.e., N, can be calculated as an arithmetic progression such that $N = \sum_{1\times2}^{25\times2} N_i/2 = 325$. N_{total} can exponentially increase if the transmitting coil dimension expands.

To illustrate how the MI changes as N_i varies, a portion of the conventional optimization is performed and analyzed as an example. In this example, the inner dimension of the inner coil ϕ is set to be 40 mm. The number of N_i is reduced from 25×2 to 10×2 by a step size of 1×2 from the coil outside to its center to emphasize the results. 200 mm is used as the main evaluation range of M_{eq}. As N_i decreases from 25×2 to

10×2, misalignment under 220 and 240 mm are also calculated for supplementary evaluations.

To improve the coil misalignment tolerant capability, all M_{eq} from 0 mm to 200 mm should be as stable as possible. In Fig. 5(d), M_{lp2ls} dominates M_{eq} when $N_{\mathrm{i}} = 25 \times 2$. By reducing N_{i} from 25×2 to 18×2, M_{eq} curves gradually become stable. Based on (21) and Fig. 5(d), it can be observed that M_{lp2ls} changes in proportion to N_{i}. Therefore, it can be derived that as 40 mm is the minimum allowed internal dimension of the inner coil, by making $\phi = 40$ mm and setting the outside dimension of each coil as $D_k = 40 + 2N_{\mathrm{i}} \times a$, where $k = 1, 2, 3, \ldots\ n$, the inner coil obtains its maximum coverage under each D_k. M_{lp2ls} reaches its maximum and corresponding M_{eq} curve reaches minimum under each D_k. By reducing N_{i} or increasing ϕ, M_{lp2ls} decreases and M_{eq} curves ascend. Thus, all inner coil designs under $N_{\mathrm{i}} < 18 \times 2$ in Fig. 5(d) cannot achieve a stable M_{eq}. Inner coil designs within $18 \times 2 \leq N_{\mathrm{i}} \leq 25 \times 2$ and $\phi = 40$ mm condition can be further optimized by reducing the coil coverage and are marked with green shadow in Fig. 5(d).

In the conventional optimization method, all the coil design dimensions are calculated without screening. The optimization efficiency can be improved by considering the aforementioned fact that M_{eq} curve ascends by reducing N_{i} or increasing ϕ, such that dimensions with higher MI curve output than the flat curve can be excluded before the optimization calculation, i.e., D_k under $N_{\mathrm{i}} < 18 \times 2$ in this case.

To make use of the aforementioned MI variation regulations, an algorithm is proposed to improve the optimization efficiency, by which most of the designs incapable of offering a stable equivalent MI are excluded at an early stage and the number of problems to be solved is reduced without compromising the accuracy. Both square and circular inner coil designs are considered and compared for the optimization.

As shown in Fig. 6, the optimization is initiated by setting the operating frequency *f*, distance *d*, dimensions and number of turns of the transmitting and receiving coils. The optimization algorithm can be summarized in the three following stages, as shown in Fig. 6.

1) Prescreening the inner coil dimensions to be calculated. By fixing the inside dimension at $\phi = 40$ mm and reducing N_{i} from 25×2 by a step size of 1×2, the maximum inner coil coverage under each D_k is obtained and $M_{\mathrm{eq}_m}(m = 0, 20, 40, \ldots\ 240\,\mathrm{mm})$ reaches minimum under each D_k. $M_{\mathrm{eq0}} \leq M_{\mathrm{eq200}}$ is used to ensure that M_{eq_m} curve can further ascend by reducing N_{i} or increasing ϕ. This step removes all D_ks that are already beyond the flat curve at the first stage. The results are identical to Fig. 5(d) in which N_{i} from 25×2 to 18×2 are within the optimization range and all $N_{\mathrm{i}} < 18 \times 2$ combinations are excluded. The outside lengths of the inner coil satisfying $M_{\mathrm{eq0}} \leq M_{\mathrm{eq200}}$ are stored and calculated as D_k. For example, $D_1 = 40 + 2 \times 25 \times 2 \times a$ when $N_{\mathrm{i}} = 25 \times 2$ and $D_8 = 40 + 2 \times 18 \times 2 \times a$ when $N_{\mathrm{i}} = 18 \times 2$.
2) Standard derivation calculation of possible designs within each D_k. As D_k is the outer dimension of the inner coil, ϕ can be increased by reducing N_{i} from inside of the coil and $M_{\mathrm{eq}m}$ can be increased. By reducing N_{i} from inside of the coil by a step size of 2 while ensuring that $M_{\mathrm{eq0}} \leq M_{\mathrm{eq200}}$, all the combinations under given D_ks are calculated. Then, $M_{\mathrm{eq}m}$ are calculated for each coil design. The standard derivation S is defined as $S = \sqrt{\frac{1}{N}\sum_{m=0}^{m=200}(M_{\mathrm{eq}m} - \mu)^2}$ to evaluate the stability of $M_{\mathrm{eq}m}$ of each design, where μ is the average $M_{\mathrm{eq}m}$ from 0 to 200 mm and *N* is the number of positions to be solved. All S values under each D_k are compared and the case with the lowest S value for each D_k is selected.
3) Final comparison for all the lowest S values obtained from step 2. The design outputs the lowest S, which is the expected final optimized design.

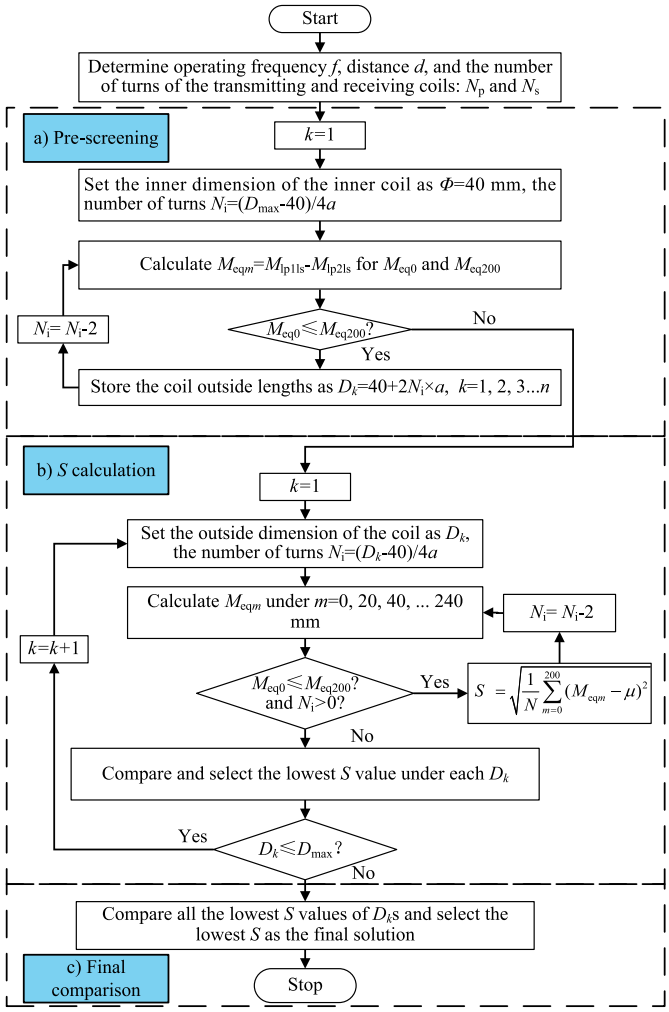

Fig. 6. Optimization flowchart for minimizing the equivalent mutual inductance differences.

As the coil design is symmetrical on both *X*- and *Y*-axes, only the *X*-axis misalignment in the range of 0 to 240 mm with a step size of 20 mm in ANSYS Maxwell is considered. The misalignment calculation range is more than half of the outer coil dimension. By running the flow chart in Fig. 6, all possible combinations capable of providing stable M_{eq} curve in the conventional optimization method are covered. Both circular and square inner coil designs are calculated and compared using

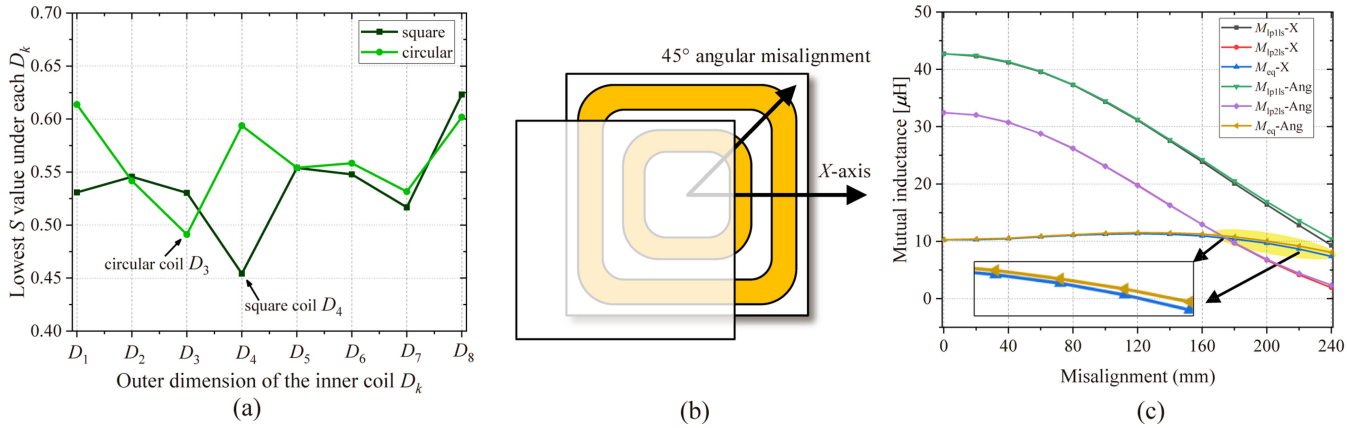

Fig. 7. Optimization results and misalignment tolerance verification setting. (a) Lowest S value under each D_k of square and circular coils. (b) Illustration of misalignment on both *X*-axis and XY-misalignment. (c) MI and equivalent MI values of the coil with the lowest standard derivation under *X*-axis and XY-misalignment.

the proposed optimization algorithm. The lowest S values under each D_k of circular and square inner coils are provided in Fig. 7(a). The circular inner coil design outputs the lowest S of 0.4911 at D_4, while the square inner coil design outputs the lowest S of 0.4524 at D_3. Therefore, square inner coil design is selected as it achieves the most stable output in terms of S. The optimized design is, thus, a square inner coil with $N_{\mathrm{i}} = 9 \times 2$ and $D_3 = 304$ mm.

Considering the fact that parking errors occur randomly on both *X*- and *Y*-directions, namely XY misalignment, instead of a single axis, which is a worst-case misalignment condition to be analyzed. Square coil designs are inherently immune to the rotational misalignments thanks to their geometrical symmetry along the rotation angle. Therefore, rotational misalignments are not disscussed in this article. To verify the misalignment tolerant capability of the optimized coil in practice, the MI and M_{eq} under *X*-axis and XY misalignment are calculated to make a comparison, as illustrated in Fig. 7(b). Equal X and Y misalignment components are used to make diagonal XY misalignment with a step size of 20 mm both in the calculation and experiment as an example. The MI and M_{eq} of the best design under *X*-axis and XY misalignments are labeled with "$-$X" and "$-$XY", respectively, as shown in Fig. 7(c). It can be observed that under *X*-axis misalignment, $M_{\mathrm{eq-X}}$ under specific misalignment positions is slightly higher than that under 0 mm position. The results of XY misalignment show a similar stable output due to the fact that the coil design is symmetrical, and the XY misalignment can be decomposed into *X*- and *Y*-axes with the same misalignment tolerant capability. Under an ideal condition, XY misalignment tolerant range in Fig. 7(b) can be $200 \times \sqrt{2}$ mm. However, due to the fillet of the inner coil as shown in Fig. 5(a) and (b), the misalignment tolerant range is close to 200 mm but it reduces more slowly from 200 to 240 mm compares to *X*-axis misalignment. The optimization algorithm enables the design to output similar misalignment tolerance under both *X*-axis and XY misalignment.

To evaluate the optimization efficiency improvement, the numbers of combinations to be calculated under each D_k using the proposed and conventional optimization algorithms are provided and compared in Table I. The $M_{\mathrm{eq0}} \leq M_{\mathrm{eq200}}$ criteria helps reduce the problems to be solved from D_1 to D_8 without impacting the accuracy. It also removes all the calculations from D_9 to D_{25} as analyzed in Fig. 5(d), while they are calculated in the conventional method and the number totals to be 153. It can be observed from Table I that the number of problems to be solved reduces from 325 to 62 by using the proposed optimization method, which offers 80.92% improvement in optimization efficiency without compromising the accuracy.

IV. Analysis of Magnetic Field Distribution

To evaluate the field enhancement performance and flux leakage of the proposed coil design, the magnetic flux density of the proposed overlapped integration coil, the proposed coil in single-layer and double-layer configurations without the inner coil are calculated. The excitation current in each coil is set to be 23 A based on the peak current from the experimental results in Section V. The magnetic flux density distributions over the top surface of the three coil designs are provided in Fig. 8 by applying the color scale on the left, ranging from 0.1 to 22 mT. The plotting areas in Fig. 8 are all the same to make fair comparisons. According to the Biot–Savart law and the magnetic field superposition principle, B as the transmission magnetic flux density, is proportional to the current in each coil. The magnetic flux density within the transmission area is twice, which is the foundation of the field enhancement. The field enhancement results are verified by Fig. 8, where the proposed overlapped integration design in Fig. 8(a) shows the highest flux density within the coil. Quantitative comparisons of the field enhancement results are discussed later.

To compare the flux leakage, the 0.14 mT color scale is selected as a sufficiently small color scale to be the boundary of the magnetic flux distributions, and is highlighted in red in Fig. 8. It can be observed that the flux distribution boundary of the proposed overlapped integration design in Fig. 8(a) is larger than that of the proposed coil design in single-layer, however, it is

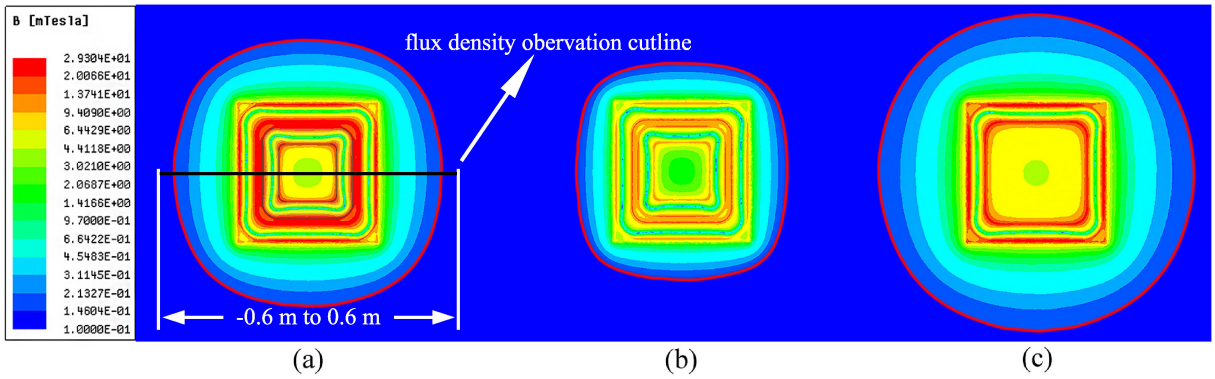

Fig. 8. Magnetic flux density distribution over the top surface of the transmitting coil. (a) Proposed overlapped integration coil design. (b) Single-layer misalignment tolerant coil. (c) Overlapped coil without any inner coil.

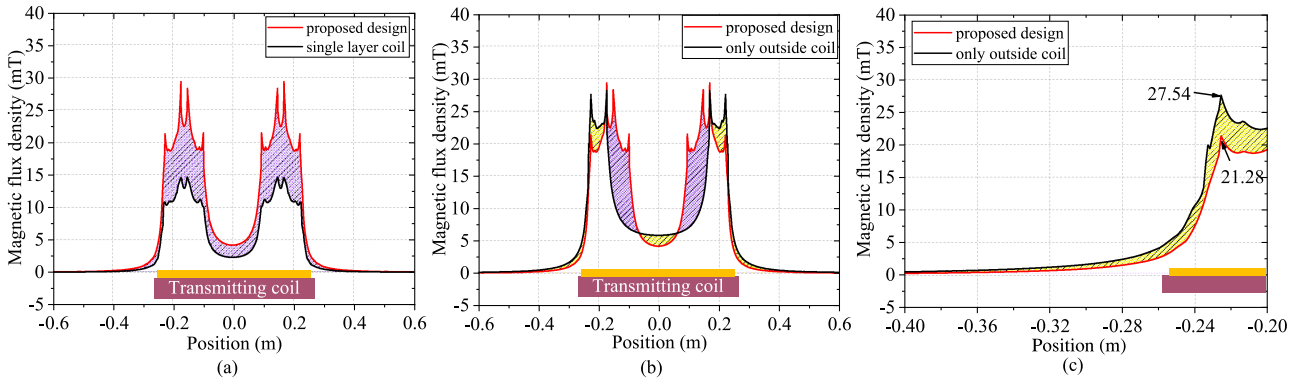

Fig. 9. Magnetic flux density along the cutline on the top surface of the primary coils from −0.6 m to 0.6 m on *X*-axis. (a) Proposed integration design versus the single-layer coil. (b) Proposed integration design versus double-layer outer coils. (c) Leakage flux intensity of the proposed integration design versus the overlapped coil without the inner coil.

still much smaller than that of the double-layered unipolar coils, as illustrated in Fig. 8(c). The leakage field reduction is due to the reverse connection nature of the inner coil, which generates the magnetic field in a reverse direction outside the transmission area such that a part of the flux leakage is canceled. Therefore, the inner coil design helps reduce the flux emissions outside of the coil area of the overlapped integration design.

To quantitatively compare the magnetic flux density distribution, the magnetic flux density is plotted along a cutline through the center of each coil from −0.6 to 0.6 in Fig. 8. The cutline is illustrated in Fig. 8(a), which is on the top surface of each transmitting coil. The magnetic flux density values on the cutline are provided in Fig. 9, where the position on the cutline is plotted as the horizontal axis. It can be observed from Fig. 9(a) that the integrated coil design, as compared to the single-layer coil within the coil, strengthens the flux density, which is the basis of the field enhancement. Fig. 9(b) shows that compared to the double-layered unipolar coil, the proposed design enables enhanced flux density within the power transmission area, displayed by the slanted line in Fig. 9(b). Outside of the power transmission area, shown by the yellow slanted line, the flux leakage is reduced. Fig. 9(c) shows that the leakage flux density of the proposed design outside of the transmission area is always lower than the design without any inner coil. The maximum magnetic flux leakage reduction reaches 22.73% at the outside boundary of the coil. Therefore, it can be concluded that the proposed integration design enhances the magnetic flux density within the same coil surface, while it can still maintain less leakage field compared to the conventional double-layered transmitter without the inner coil.

V. Experimental Results

A. Experimental Setup and Parameter Variation Analysis

To validate the proposed design and analysis, a 1-kW field enhanced integrated WPT prototype is fabricated. The parameters of the prototype are provided in Table II. The coil dimensions and the nominal gaps between the pads are selected based on the reference design of SAE J2954 [29] and the optimization results. Polyethylene foam, which is magnetically transparent and similar to air, is used to create the distance while isolating the coils.

The compensation coil L_{f} is shown in Fig. 10(a). The transmitting coil L_{p} is identical to the compensation coil. L_{f} and L_{p} are tightly attached to each other and are placed on the lower ferrite layer. The receiving coil is shown in Fig. 10(b), and ferrite

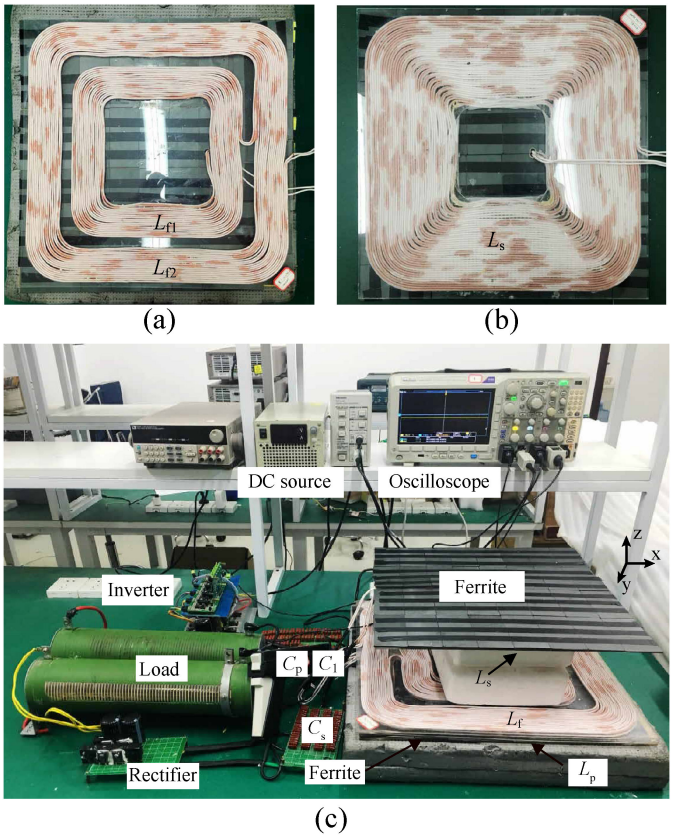

Fig. 10. Experimental setup. (a) Compensation coil. (b) Receiving coil. (c) Overall system setup.

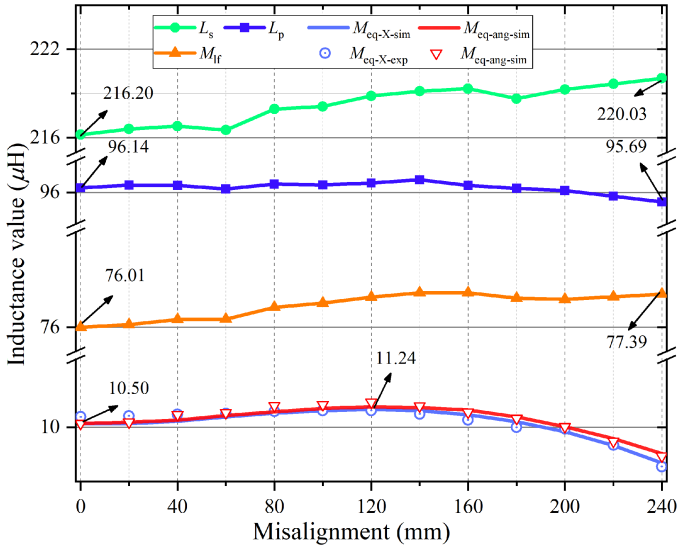

Fig. 11. Inductance and MI values of the corresponding coils under misalignment.

tiles are also placed on the top of the receiving coil. Fig. 10(c) shows the system setup profile where an adjustable resistor is used as the load.

To analyze the parameter sensitivity of the inductance and MI values for each coil under misalignment, the corresponding inductance and MI values are measured under misalignment varying from 0 to 240 mm with a step size of 20 mm on the *X*-axis. The MI variation under XY misalignment in Fig. 7(b) is also performed. The corresponding inductance values are plotted in Fig. 11, where the vertical axis is inserted with breaks to emphasize the results. It can be noticed from the results that the inductance values of $L_{\rm p}$, $L_{\rm s}$, and $M_{\rm lf}$ are almost constant and the variations can be ignored under misalignment. For example, the inductance value of $L_{\rm s}$ is 216.20 μH without misalignment while it increases to 220.03 μH under 240 mm misalignment. The variation compared to its nominal position is 1.77%. $L_{\rm p}$ changes from 96.14 μH under 0 mm to 95.69 μH under 240 mm misalignment, which varies only 0.46% compared to its nominal value. $M_{\rm lf}$ also changes as low as 1.82% from 76.01 μH to 77.39 μH when misalignment changes from 0 mm to 240 mm. As the changes are small, these values are considered as constant.

$M_{\rm eq}$ under *X*-axis and XY misalignments are labeled with "$-$X" and "$-$XY". "$-$sim" and "$-$exp" are used to indicate the simulation and experimental results, respectively. It can be observed from the simulation results that $M_{\rm eq-X-sim}$ is close to $M_{\rm eq-XY-sim}$ from 0 to 140 mm, while $M_{\rm eq-XY-sim}$ declines much slower than $M_{\rm eq-X-sim}$ from 160 to 240 mm. The experimental results of $M_{\rm eq}$ are closely matched with the simulation results and the values are stable from 0 to 200 mm.

It should be noted that, even though both the compensation and the transmitting coils are identical and tightly attached to each other, the distances between the lower ferrite layer to the compensation and the transmitting coils are slightly different. The ferrite layer impacts the coil inductance value and, thus, the inductance value of each coil, to some extent, is different. Under identical coil design, the coil closer to the ferrite layer would have a slightly higher inductance (due to the smaller distance to the ferrites). In the experiment, the nominal inductance value of the compensation coil $L_{\rm f}$ is 83.12 μH, while the nominal inductance value of the transmitting coil $L_{\rm p}$ is 96.14 μH. The small inductance difference between $L_{\rm f}$ and $L_{\rm p}$, due to the identical coil design sharing the same ferrite layer, is unavoidable. Adding extra turns to $L_{\rm f}$, which is on the top layer, is a solution to compensate the inductance difference. However, the accurate amount of turns needs to be determined by measuring the coil during the fabrication process, which is not straightforward. To simplify the experimental implementation, the capacitor C_1 is used to be connected in series with $L_{\rm p}$ to match the inductance imbalance, as shown in Fig. 11. $L_{\rm pe}$ is the equivalent inductance after C_1 compensation such that $L_{\rm pe} = L_{\rm f}$. With this approach, number of turns and the coil diameters can remain identical and the topology still works as an *LCL-S* circuit.

B. Operation Analysis

The input voltage and current waveforms of each branch under the nominal load condition at 0 mm misalignment are provided in Fig. 13. It can be observed from $V_{\rm in}$ and $I_{\rm f}$ in Fig. 13(a), the input ZPA is achieved at 85 kHz. The input of the rectifier waveforms are also displayed in Fig. 13(a), in

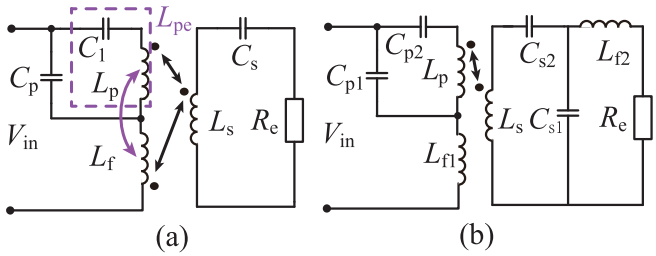

Fig. 12. Equivalental experimental circuit considering parameter imperfection. (a) Proposed design with capacitor C_1. (b) *LCC* circuit.

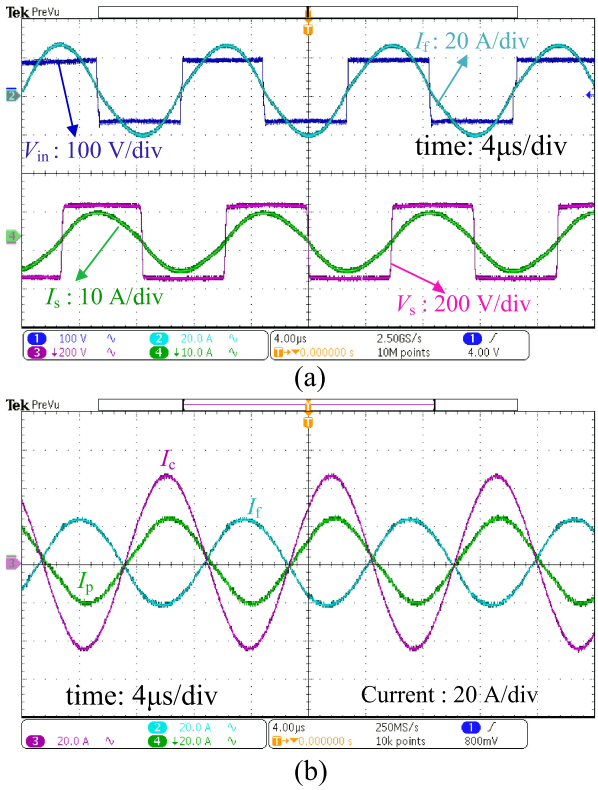

Fig. 13. Steady-state waveforms when delivering 1 kW power with $V_{in} = 65$ V. (a) Output voltage and current waveforms of the corresponding branches. (b) Coil currents I_f, I_p, and I_s.

which the phase of each waveform is verified by (9). The field enhancement design is also validated by the current waveform of each branch on the primary side, provided in Fig. 13(b). I_p and I_f are in the opposite phases and there is only $5.71°$ phase shift from the perfect opposite. Both currents have the same magnitude and are superpositioned as I_c. The phase difference is impacted by the load and originates from the small fractions ignored in the simplification of the analysis. It is still small enough to be ignored under operation and can be improved if the load resistance increases, according to the analysis in Section II.

As the load impedance may vary during the operation, CC output characteristics are measured in Fig. 14. Since there is no common recognized resistance value for EV charging in the literature, the resistance value is selected as 40 Ω based on the design examples in [27] and [21]. V_r and I_s are measured with

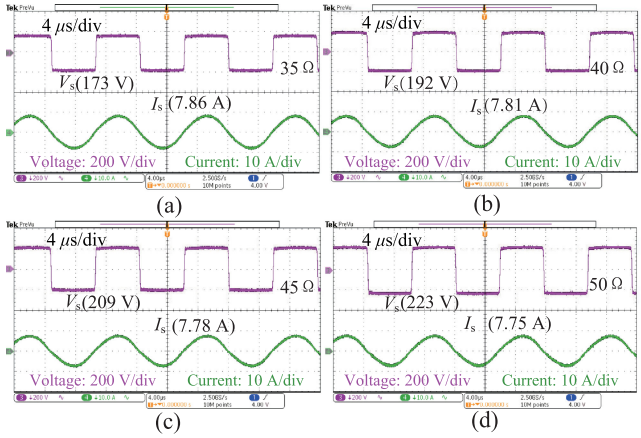

Fig. 14. CC verification under load variations: (a) $R = 35$ Ω; (b) $R = 40$ Ω; (c) $R = 45$ Ω; and (d) $R = 50$ Ω.

R varying around 40 Ω. It can be observed that I_r changes from 7.86 A to 7.75 A as the load increases from 35 Ω to 50 Ω, which is only 1.39% current variation under a relatively wide load changes in battery charging.

C. Comparison Between the Proposed Design and the Conventional LCC Circuit

Even though the proposed design is based on the *LCL* circuit, based on the proposed integration and compensation design, its output characteristic changes from CV to CC. In addition, according to (20d), the power transfer capacity of the proposed design is amplified compared to the conventional *LCL* circuit. Under the same transmitting and receiving coils arrangement, it is difficult to adjust the output power of the conventional *LCL* circuit to the same level of the proposed design as the compensation and transmitting inductor values are identical, whereas double-sided *LCC* can be easily adjusted by varying L_{f1} and L_{f2} values in (20b). Therefore, to make a fair comparison, the proposed design is compared with the double-sided *LCC* with CC output in the experiment. As M_{eq} curves under *X*-axis and XY misalignments are similar in Fig. 11, the experiments are performed under *X*-axis misalignments for simplification.

The experiment is carried out under *X*-axis misalignment varying from 0 to 240 mm with a step size of 20 mm. The output power and efficiency under each position are measured. The experimental circuit diagram of the *LCC* circuit is provided in Fig. 12(b), where L_{f1} is decoupled from L_p or L_s. Using the same transmitting and receiving coils used in the proposed system, identical L_{f1} and L_{f2} can be calculated from (20e) to output the same power with the proposed system. The parameters of the double-sided *LCC* circuit are listed in Table III.

The system efficiency as well as the output power of the *LCC* circuit are provided in Fig. 15. Due to imperfection of the parameters, the system efficiency reaches 90.45% under the nominal condition while the output power is 998.96 W. The efficiency stays stable as misalignment increases from 0 mm to 200 mm, while the output power fluctuates in proportion to the equivalent $M_{eq-X-exp}$ values in Fig. 11. As misalignment

TABLE III
LCC-LCC CIRCUIT PARAMETERS

Symbol	Description	Value
L_{f1}	Compensation coil inductance on the primary side	14.51 μH
L_p	Transmitting coil inductance	96.14 μH
L_s	Receiving coil inductance	216.04 μH
L_{f2}	Compensation coil inductance on the secondary side	14.58 μH
M_{eq}	Nominal equivalent MI	10.78 μH
R	Load resistance	40 Ω
C_{p1}	Capacitor on the primary side	252.42 nF
C_{p2}	Capacitor on the primary side	45.59 nF
C_{s1}	Capacitor on the receiving side	253.31 nF
C_{s2}	Capacitor on the receiving side	17.43 nF

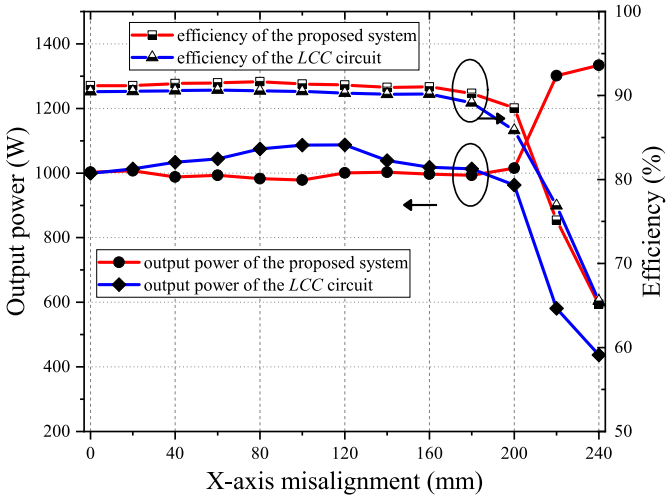

Fig. 15. System efficiency and output power comparison between the proposed design and the double-sided *LCC* circuit.

increases from 200 mm to 240 mm, the system efficiency reduces from 85.84% to 65.52% while the output power reduces from 967.38 W to 441.11 W.

The experimental results of the proposed integrated system are also provided in Fig. 15. As shown, the proposed design outputs similar efficiency and power compared to the *LCC* circuit when there is no misalignment. The proposed system achieves 91.17% as its system efficiency while the output power reaches 1003.27 W under the nominal condition. Both the efficiency and output power are stable within the designed misalignment tolerant range from 0 to 200 mm. Under a large misalignment, i.e., from 200 to 240 mm, M_{eq} decreases, which results in increased output power and can be explained by (20c). The output power increase under a low MI is due to the increased input current on the primary side, which can be explained by (16a). Under 240 mm misalignment, the MI decreases to 7.11 μH such that the output power reaches 1333.98 W and the efficiency decreases to 65.23%. It should be noted that the output power increase, as MI decreases, can be considered a drawback under a large misalignment. Series-series and series-parallel tuned WPT systems have the same exact behavior [6], [7]. With the larger airgap or higher misalignment, the mutual inductance decreases;

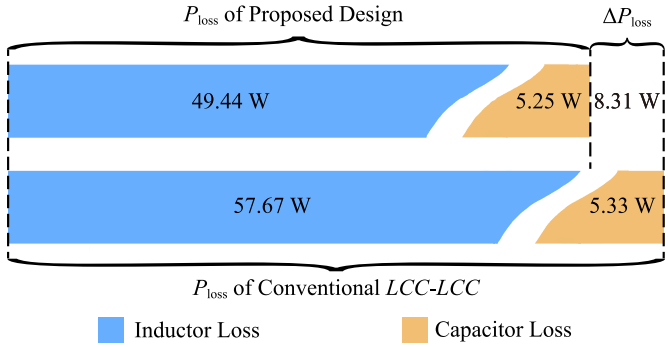

Fig. 16. Comparison of power loss distributions in resonant components.

resulting in a higher primary coil and magnetizing branch current in the system, which in turn induces more voltage on the secondary side. This behavior exists to an extent for a minimum value of the coupling factor or mutual inductance. A coupling factor or mutual inductance value lower than this minimum level would result in reduced power transfer. In case of significant power increase when the receiving coil is not within the designed operation range, a protection or detection circuit can be used as in some other CC output circuits with a voltage source input [6].

As both the conventional *LCC* circuit and the proposed design use the same inverter and rectifier, the converter losses of both systems are identical and unavoidable under 0 mm misalignment nominal operation, therefore, is not discussed here. The power losses of the resonant tank include inductance loss and capacitor loss. The power losses can be easily obtained by measuring the resistance of the resonant components and their corresponding resonant current under 0 mm misalignment operation. The comparison of power loss distribution of the resonant components is shown in Fig. 16, where P_{loss} is the power loss of the resonant components and ΔP_{loss} is the power loss difference between the conventional *LCC* circuit and the proposed design. It can be observed that the inductor losses account for the most part of the power loss and capacitor losses are small and similar. The conventional *LCC* circuit performs higher system efficiency and $\Delta P_{loss} = 8.31$ W. ΔP_{loss} comes from less numbers of compensation inductors used in the proposed circuit design.

The power changing regulations of the conventional *LCC* circuit and the proposed design are closely matched with (20b) and (20c), respectively. Overall, the proposed design achieves an stable output both in terms of efficiency and power within the misalignment tolerant range. It also achieves CC output with less compensation inductors and capacitors to deliver the same power level compared with the double-sided *LCC* circuit.

VI. CONCLUSION

A magnetic integrated compensation coil design using identical coils based on an *LCL-S* compensation topology is proposed to enhance the power transfer capacity and misalignment tolerance of a WPT system. A pair of tightly coupled coils are implemented on the primary side and a new compensation

strategy featuring field enhancement, input ZPA, and load-independent output is developed. The proposed structure spares space and magnetic cores outside of the coupler, which are normally needed for the compensation inductors. The feasibility of the proposed topology is investigated through the equivalent circuit modeling and analysis. The characteristics of the proposed integrated design, especially the extra integration-induced couplings, are modeled and studied by FEA. By adopting the misalignment tolerant coil, the proposed system offers uniform misalignment tolerance under random horizontal parking errors. An optimization algorithm is also developed to reduce the significant number of FEA trials to a reasonable low-scale number and to expedite the design process. The proposed structure and corresponding analyses are validated through experiments on a scaled-down prototype.

REFERENCES

[1] A. Ahmad, M. S. Alam, and R. Chabaan, "A comprehensive review of wireless charging technologies for electric vehicles," *IEEE Trans. Transp. Electrific.*, vol. 4, no. 1, pp. 38–63, Mar. 2018.

[2] G. A. Covic and J. T. Boys, "Inductive power transfer," *Proc. IEEE*, vol. 101, no. 6, pp. 1276–1289, Jun. 2013.

[3] D. Vincent, P. S. Huynh, N. A. Azeez, L. Patnaik, and S. S. Williamson, "Evolution of hybrid inductive and capacitive ac links for wireless EV charging—a comparative overview," *IEEE Trans. Transp. Electrific.*, vol. 5, no. 4, pp. 1060–1077, Dec. 2019.

[4] S. Y. R. Hui, W. Zhong, and C. K. Lee, "A critical review of recent progress in mid-range wireless power transfer," *IEEE Trans. Power Electron.*, vol. 29, no. 9, pp. 4500–4511, Sep. 2014.

[5] J. P. W. Chow, N. Chen, H. S. H. Chung, and L. L. H. Chan, "An investigation into the use of orthogonal winding in loosely coupled link for improving power transfer efficiency under coil misalignment," *IEEE Trans. Power Electron.*, vol. 30, no. 10, pp. 5632–5649, Oct. 2015.

[6] Y. H. Sohn, B. H. Choi, E. S. Lee, G. C. Lim, G. Cho, and C. T. Rim, "General unified analyses of two-capacitor inductive power transfer systems: Equivalence of current-source SS and SP compensations," *IEEE Trans. Power Electron.*, vol. 30, no. 11, pp. 6030–6045, Nov. 2015.

[7] W. Zhang, S. Wong, C. K. Tse, and Q. Chen, "Design for efficiency optimization and voltage controllability of series-series compensated inductive power transfer systems," *IEEE Trans. Power Electron.*, vol. 29, no. 1, pp. 191–200, Jan. 2014.

[8] G. Buja, M. Bertoluzzo, and K. N. Mude, "Design and experimentation of WPT charger for electric city car," *IEEE Trans. Ind. Electron.*, vol. 62, no. 12, pp. 7436–7447, Dec. 2015.

[9] S. Li and C. C. Mi, "Wireless power transfer for electric vehicle applications," *IEEE J. Emerg. Sel. Topics Power Electron.*, vol. 3, no. 1, pp. 4–17, Mar. 2015.

[10] Z. Pantic, S. Bai, and S. M. Lukic, "ZCS LCC-compensated resonant inverter for inductive-power-transfer application," *IEEE Trans. Ind. Electron.*, vol. 58, no. 8, pp. 3500–3510, Aug. 2011.

[11] S. Li, W. Li, J. Deng, T. D. Nguyen, and C. C. Mi, "A double-sided LCC compensation network and its tuning method for wireless power transfer," *IEEE Trans. Veh. Technol.*, vol. 64, no. 6, pp. 2261–2273, Jun. 2015.

[12] X. Qu, Y. Jing, H. Han, S. Wong, and C. K. Tse, "Higher order compensation for inductive-power-transfer converters with constant-voltage or constant-current output combating transformer parameter constraints," *IEEE Trans. Power Electron.*, vol. 32, no. 1, pp. 394–405, Jan. 2017.

[13] W. Li, H. Zhao, S. Li, J. Deng, T. Kan, and C. C. Mi, "Integrated lcc compensation topology for wireless charger in electric and plug-in electric vehicles," *IEEE Trans. Ind. Electron.*, vol. 62, no. 7, pp. 4215–4225, Jul. 2015.

[14] H. Zhang, C. Zhu, and F. Lu, "A compact and low-distortion inductive charging system for automatic guided vehicles based on LCC compensation and integrated magnetic coupler," in *Proc. IEEE Transp. Electrific. Conf. Expo.*, Jun. 2019, pp. 1–5.

[15] T. Kan, T. Nguyen, J. C. White, R. K. Malhan, and C. C. Mi, "A new integration method for an electric vehicle wireless charging system using LCC compensation topology: analysis and design," *IEEE Trans. Power Electron.*, vol. 32, no. 2, pp. 1638–1650, Feb. 2017.

[16] T. Kan, F. Lu, T. Nguyen, P. P. Mercier, and C. C. Mi, "Integrated coil design for EV wireless charging systems using LCC compensation topology," *IEEE Trans. Power Electron.*, vol. 33, no. 11, pp. 9231–9241, Nov. 2018.

[17] J. Deng, W. Li, T. D. Nguyen, S. Li, and C. C. Mi, "Compact and efficient bipolar coupler for wireless power chargers: design and analysis," *IEEE Trans. Power Electron.*, vol. 30, no. 11, pp. 6130–6140, Nov. 2015.

[18] W. Gao, L. Jiang, Q. Chen, X. Ren, Z. Zhang, and S. Wong, "Analysis and design of an integrated LCL-S contactless resonant converter," in *Proc. IEEE Appl. Power Electron. Conf. Expo.*, Mar. 2018, pp. 3178–3182.

[19] Z. Yan *et al.*, "Fault-tolerant wireless power transfer system with a dual-coupled LCC-S topology," *IEEE Trans. Veh. Technol.*, vol. 68, no. 12, pp. 11 838–11 846, Dec. 2019.

[20] V. Vu, V. Phan, M. Dahidah, and V. Pickert, "Multiple output inductive charger for electric vehicles," *IEEE Trans. Power Electron.*, vol. 34, no. 8, pp. 7350–7368, Aug. 2019.

[21] Y. Jiang, L. Wang, Y. Wang, J. Liu, M. Wu, and G. Ning, "Analysis, design, and implementation of WPT system for EV's battery charging based on optimal operation frequency range," *IEEE Trans. Power Electron.*, vol. 34, no. 7, pp. 6890–6905, Jul. 2019.

[22] A. Tejeda, S. Kim, F. Y. Lin, G. A. Covic, and J. T. Boys, "A hybrid solenoid coupler for wireless charging applications," *IEEE Trans. Power Electron.*, vol. 34, no. 6, pp. 5632–5645, Jun. 2019.

[23] Y. Liu, R. Mai, D. Liu, Y. Li, and Z. He, "Efficiency optimization for wireless dynamic charging system with overlapped DD coil arrays," *IEEE Trans. Power Electron.*, vol. 33, no. 4, pp. 2832–2846, Apr. 2018.

[24] O. Onar *et al.*, "Modeling, design, and experimental verification of a WPT level-3 wireless charger with compact secondary coupler," in *Proc. IEEE Appl. Power Electron. Conf. Expo.*, Mar. 2019, pp. 1722–1729.

[25] A. Kamineni, G. A. Covic, and J. T. Boys, "Analysis of coplanar intermediate coil structures in inductive power transfer systems," *IEEE Trans. Power Electron.*, vol. 30, no. 11, pp. 6141–6154, Nov. 2015.

[26] Y. Li, J. Zhao, Q. Yang, L. Liu, J. Ma, and X. Zhang, "A novel coil with high misalignment tolerance for wireless power transfer," *IEEE Trans. Magn.*, vol. 55, no. 6, pp. 1–4, Jun. 2019.

[27] Y. Chen, R. Mai, Y. Zhang, M. Li, and Z. He, "Improving misalignment tolerance for IPT system using a third-coil," *IEEE Trans. Power Electron.*, vol. 34, no. 4, pp. 3009–3013, Apr. 2019.

[28] J.-M. Jin, *The Finite Element Method in Electromagnetics*. New York, NY, USA: Wiley, 2015.

[29] S. Standard, "J2954, wireless power transfer for light-duty plug-in electric vehicles and alignment methodology," SAE J2954 TIR, 2017.

[30] W. Zhang and C. C. Mi, "Compensation topologies of high-power wireless power transfer systems," *IEEE Trans. Veh. Technol.*, vol. 65, no. 6, pp. 4768–4778, Jun. 2016.

[31] Y. Li, T. Lin, R. Mai, L. Huang, and Z. He, "Compact double-sided decoupled coils-based WPT systems for high-power applications: analysis, design, and experimental verification," *IEEE Trans. Transp. Electrific.*, vol. 4, no. 1, pp. 64–75, Mar. 2018.

[32] B. Esteban, M. Sid-Ahmed, and N. C. Kar, "A comparative study of power supply architectures in wireless EV charging systems," *IEEE Trans. Power Electron.*, vol. 30, no. 11, pp. 6408–6422, Nov. 2015.

[33] Y. Jiang, L. Wang, Y. Wang, J. Liu, X. Li, and G. Ning, "Analysis, design, and implementation of accurate ZVS angle control for EV battery charging in wireless high-power transfer," *IEEE Trans. Ind. Electron.*, vol. 66, no. 5, pp. 4075–4085, May 2019.

[34] J. Sallan, J. L. Villa, A. Llombart, and J. F. Sanz, "Optimal design of ICPT systems applied to electric vehicle battery charge," *IEEE Trans. Ind. Electron.*, vol. 56, no. 6, pp. 2140–2149, Jun. 2009.

[35] G. Rituraj, B. K. Kushwaha, and P. Kumar, "A unipolar coil arrangement method for improving the coupling coefficient without ferrite material in wireless power transfer systems," *IEEE Trans. Transp. Electrific.*, vol. 6, no. 2, pp. 497–509, Jun. 2020.

[36] C. Cai, J. Wang, H. Nie, P. Zhang, Z. Lin, and Y. Zhou, "Effective-configuration WPT systems for drones charging area extension featuring quasi-uniform magnetic coupling," *IEEE Trans. Transp. Electrific.*, vol. 6, no. 3, pp. 920–934, Sep. 2020.

[37] N. E. W. Technology, "Product selection guide," May 2016. [Online]. Available: https://s3-us-east-2.amazonaws.com/newtcdn/wp-content/uploads/2018/03/1 6104646/NEW_Catalog.pdf

[38] C. R. Paul, *Inductance: Loop and Partial*. New York, NY, USA: Wiley, 2011.

Pengcheng Zhang (Member, IEEE) was born in Anhui, China, in 1991. He received the B.S. degree in electrical engineering and the M.S. degree in control science and engineering from Tianjin Polytechnic University, Tianjin, China, in 2013 and 2016, respectively. He is currently working toward the Ph.D. degree in electrical engineering with the Hebei University of Technology, Tianjin, China.

From November 2017 to December 2019, he was a Visiting Researcher with the School of Electrical and Computer Engineering, Georgia Institute of Technology, Atlanta, GA, USA. His current research interests include engineering electromagnetism, wireless power transfer, and its industrial applications.

Maryam Saeedifard (Senior Member, IEEE) received the Ph.D. degree in electrical engineering from the University of Toronto, Toronto, ON, Canada, in 2008.

She is currently as Associate Professor with the School of Electrical and Computer Engineering, Georgia Institute of Technology, Atlanta, GA, USA. Her research interests include power electronics and applications of power electronics in power systems.

Omer C. Onar (Senior Member, IEEE) received the Ph.D. degree in electrical engineering from the Illinois Institute of Technology, Chicago, IL, USA, in 2010.

Dr. Onar was the recipient of the Department of Energy Vehicle Technologies Office Distinguished Achievement Team Award and UT-Battelle Research Accomplishment Team Award for his work on wireless power transfer systems in 2016. In July 2010, he received the Alvin M. Weinberg Fellowship at the U.S. Department of Energy's Oak Ridge National Laboratory, where he joined the Power Electronics and Electric Machinery Group. At Oak Ridge National Laboratory, he has been working on advanced power electronics and electric drives, renewable energies, energy storage systems, wireless power transfer systems, and smart grids. He is an Associate Editor for the IEEE TRANSACTIONS ON TRANSPORTATION ELECTRIFICATION and IEEE TRANSACTIONS ON POWER ELECTRONICS. He also received an R&D 100 Award jointly with Toyota TEMA for the wireless charging of EVs project in 2016.

Qingxin Yang received the B.S., M.S., and Ph.D. degrees from the Hebei University of Technology, Tianjin, China, in 1983, 1986, and 1997, respectively.

Since 1996, he has been a Professor with the Hebei University of Technology. From 2008 to 2018, he was the President of Tianjin Polytechnic University, China. Since 2018, he has been the President of Tianjin University of Technology, China. His research interests include computational electromagnetism, engineering electromagnetism and their applications, and special wireless power transfer.

Dr. Yang was a Board Member of International COMPUMAG Society and the President of China chapter. Since 2015, he has been the President of China Electrotechnical Society.

Changsong Cai (Member, IEEE) was born in Henan, China, in 1992. He received the B.S. degree in electrical engineering from Tianjin Polytechnic University, Tianjin, China, in 2014, and the M.Eng. degree in electrical engineering in 2017 from Wuhan University, Wuhan, China, where he is currently working toward the Ph.D. degree in electrical engineering.

Since October 2019, he has been a Visiting Researcher with the School of Electrical and Computer Engineering, Georgia Institute of Technology, Atlanta, GA, USA. His current research interests include applied electromagnetics and power electronics, the research main involves wireless power transfer, and its industrial applications.